

# Expansive components in H II regions

M. Relaño<sup>1</sup> and J. E. Beckman<sup>1,2</sup>

<sup>1</sup> Instituto de Astrofísica de Canarias, C. Vía Láctea s/n, 38200, La Laguna, Tenerife, Spain  
e-mail: mpastor@ll.iac.es

<sup>2</sup> Consejo Superior de Investigaciones Científicas (CSIC), Spain  
e-mail: jeb@ll.iac.es

Received 22 July 2004 / Accepted 5 October 2004

**Abstract.** We study the presence of low intensity high velocity components, which we have termed *wing* features in the integrated H $\alpha$  emission line profiles of the H II region populations of the spiral barred galaxies NGC 1530, NGC 3359 and NGC 6951. We find that more than a third of the H II region line profiles in each galaxy show these components. The highest fraction is obtained in the galaxy whose line profiles show the best S:N, which suggests that wing features of this type may well exist in most, if not all, H II region line profiles. Applying selection criteria to the wing features, we obtain a sample of H II regions with clearly defined high velocity components in their profiles. Deconvolution of a representative sample of the line profiles eliminates any doubt that the wing features could possibly be due to instrumental effects. We present an analysis of the high velocity low intensity features fitting them with Gaussian functions; the emission measures, central velocities and velocity dispersions for the red and blue features take similar values. We interpret the features as signatures of expanding shells inside the H II regions. Up to a shell radius of  $R_{\text{shell}} \sim 0.2 R_{\text{reg}}$ , the stellar winds from the central ionizing stars appear to satisfy the energy and momentum requirements for the formation and driving the shell. Several examples of the most luminous H II regions show that the shells appear to have larger radii; in these cases additional mechanisms may well be needed to explain the kinetic energies and momenta of the shells.

**Key words.** ISM: H II regions – ISM: kinematics and dynamics – galaxies: individual: NGC 1530 – galaxies: individual: NGC 6951 – galaxies: individual: NGC 3359 – galaxies: ISM

## 1. Introduction

The study of the internal kinematics of H II regions is quite difficult technically and has proved to be a far from easy task to achieve. The gas motions may be observed in the velocity profiles of the emission lines from the H II regions, which show either a broad component, typically with supersonic width, or several components. Previous studies have shown evidence of low intensity broad components in the integrated spectra of the H II regions, not only in Galactic regions but also in those in external galaxies. Arsenault & Roy (1986) found that a significant fraction of their extragalactic H II region sample showed integrated line profiles which are better characterized by a Voigt profile rather than by a single Gaussian profile; while Chu & Kennicutt (1994) and Yang et al. (1996) found the same broad component for nearby extragalactic H II regions. Up to now the interpretation of these extended components has not been studied for several reasons; the low intensity of the broad components makes it difficult to confirm their existence, and because of this, examples of H II regions showing clearly this type of components have been scarce until now.

The kinematics of nearby extragalactic H II regions, notably 30 Doradus in the LMC, and NGC 604 in M 33, have been carefully studied and have shown the existence of rapid gas

motions in their interiors. Smith & Weedman (1972) first studied the internal kinematics of 30 Doradus with Fabry-Pérot observations and found asymmetric profiles at different positions within the region; the asymmetries could be matched by fitting the line profile with several Gaussian components. Chu & Kennicutt (1994) studied the structural kinematics of 30 Doradus using several long-slit spectra to map the velocity field of the region. They concluded that the velocity field is dominated by a large number of expanding structures ranging in size and expansion velocities, most of them confined within the central zone of radius  $R \sim 65$  pc. In spite of the complex kinematic structure, the integrated velocity profile for the central part of the region, derived by adding the profiles for all the slits, shows a broad Gaussian high intensity component with faint extended wings.

Yang et al. (1996) made a similar study of NGC 604 combining CCD imaging with long-slit and Fabry-Pérot observations. They confirmed the existence of several expanding shells located in the central part of the region, as in 30 Doradus. The total H $\alpha$  luminosity coming from these shells is  $\sim 25\%$  of the total luminosity of the H II region, and the integrated velocity profile of the region shows similar faint extended wings to the profile of 30 Doradus. Other studies (Rosa & Solf 1984;

Sabalisk et al. 1995) have found the same kinematic structure of expanding shells for NGC 604.

An important question not addressed till now is whether this phenomenon can be generalized to all H II regions. Up to the present time the spatial and spectral resolution of the observations made of H II regions in galaxies outside the Local Group have not been sufficient to allow us to obtain an answer to this question. It is necessary to obtain a significant sample of H II region line profiles to make general inferences. However, the similarities between 30 Doradus and NGC 604 suggest that, in general, H II regions could well have comparable structures and internal kinematics.

In order to overcome these observational limitations, we present an analysis of the line profiles of the H II region populations of the barred spiral galaxies NGC 1530, NGC 3359 and NGC 6951 obtained using Fabry-Pérot interferometry. We confirm the existence of peaked high velocity low intensity features in a significant fraction of the line profiles and analyze a selected sample of H II regions to study further the nature of these extended wings. In providing a statistical study of the phenomenology of the wings we need to pay a very careful attention to eliminate doubts about the nature of the wings. For selected examples, we deconvolved the line profiles to obtain the best fit to the input spectra and to verify the existence of the low intensity components.

We interpret the wing features as signatures of an expanding shell within a given H II region. The energetics of the shell and the energy input requirements to produce it are studied for each H II region of a selected sample making use of representative physical parameters measured in the most luminous shells observed in the nearby H II regions, 30 Doradus and NGC 604. Finally, we have studied quantitatively the hypothesis that the expanding shells are produced by the interaction of the stellar winds coming from the ionizing stars with the ISM medium.

## 2. Observations: H II regions with wing features

### 2.1. Observations

The galaxies NGC 3359, NGC 6951 and NGC 1530 were observed with the TAURUS-II Fabry-Pérot interferometer at the 4.2 m William Herschel Telescope (WHT) on La Palma. The data reduction for each galaxy is described respectively in Rozas et al. (2000b) for NGC 3359, in Rozas et al. (2002) for NGC 6951 and in Zurita et al. (2004) for NGC 1530. The observations consist of exposures at a set of equally stepped separations of the etalon, allowing us to scan the full wavelength range of the H $\alpha$  emission line in the galaxy. For the three galaxies, the observed emission wavelengths were scanned in 55 steps with exposures times at each position of the etalon of 140 s for NGC 3359 and NGC 6951, and 150 s for NGC 1530. An appropriate redshifted narrow-band H $\alpha$  filter is used as an order-sorting filter. Wavelength and phase calibration were performed using observations of a calibration lamp before and after the exposure of the data cube. The final calibrated data cube has three axes,  $x$  and  $y$ , corresponding to the spatial coordinates in the field, and  $z$ , which corresponds to the wavelength direction. The free spectral ranges

for each galaxy (17.22 Å for NGC 3359 and NGC 6951 and 18.03 Å for NGC 1530), and the wavelength interval between consecutive planes (0.34 Å for NGC 3359 and NGC 6951 and 0.41 Å for NGC 1530), give a finesse of 21.5 for NGC 3359 and NGC 6951 and 21.2 for NGC 1530. The corresponding effective spectral resolution for our observations is close to, and slightly less, than the wavelength interval between consecutive planes, which for the data cubes from the different galaxies takes the value 15.63 km s<sup>-1</sup>, 16.66 km s<sup>-1</sup> and 18.62 km s<sup>-1</sup> for NGC 6951, NGC 3359 and NGC 1530 respectively.

From the continuum subtracted data cube we can extract line profiles of each point covered by the detector, thus we can obtain line profiles with specified apertures for any H II region in the galaxy. We assign an H $\alpha$  luminosity to the H II regions identified in the Fabry-Pérot observations using the information from the H II region catalogues of these galaxies (see Rozas et al. (1996) for NGC 6951, Rozas et al. (2000) for NGC 3359 and Relaño et al. (2004) for NGC 1530).

### 2.2. H II regions with wing features

A significant fraction (~70%) of the integrated line profiles of the H II region population in the galaxies NGC 6951, NGC 3359 and NGC 1530 are best fitted with two or three Gaussian components (Relaño et al. 2004). In this paper we focus our attention on the high velocity low intensity features detected in these H II region line profiles and in particular on those secondary Gaussian components located at more than ~35 km s<sup>-1</sup> from the centre of the most intense Gaussian component, which we will call *wing* features. A more detailed study of the central high intensity components including considerations of the possible sources of broadening of the central peaks is presented in Relaño et al. (2004).

In Fig. 1 we show some examples of line profiles with this type of features. As we can see from this figure and from the set of line profiles analyzed, the wing features appear as components symmetrically shifted in velocity with respect to the central most intense component. In order to obtain a sample of H II region line profiles with clear detected *wing* features, we have applied the following criteria. **a.** The amplitudes of the secondary components must be bigger than 2.5 times the r.m.s. noise level<sup>1</sup> of the line profile, and **b.** each secondary Gaussian component must be separated from the central one by more than 2.5 times the spectral resolution of the corresponding observed data cube. We define the spectral resolution here as the velocity separation between adjacent planes in the data cube. The values for the three galaxies are 15.63 km s<sup>-1</sup>, 16.66 km s<sup>-1</sup> and 18.62 km s<sup>-1</sup> for NGC 6951, NGC 3359 and NGC 1530, respectively, which implies separation limits in velocity of 39.08 km s<sup>-1</sup>, 41.65 km s<sup>-1</sup> and 46.55 km s<sup>-1</sup>, for NGC 6951, NGC 3359 and NGC 1530 respectively. **c.** If there is a spectrum with a single secondary Gaussian component, this must have an amplitude bigger than 3.75 times the root mean

<sup>1</sup> We define the root mean square noise level as the standard deviation of the points of the spectrum located at more than six times the distance from the peak than the velocity dispersion of the single Gaussian fitted to the line profile.

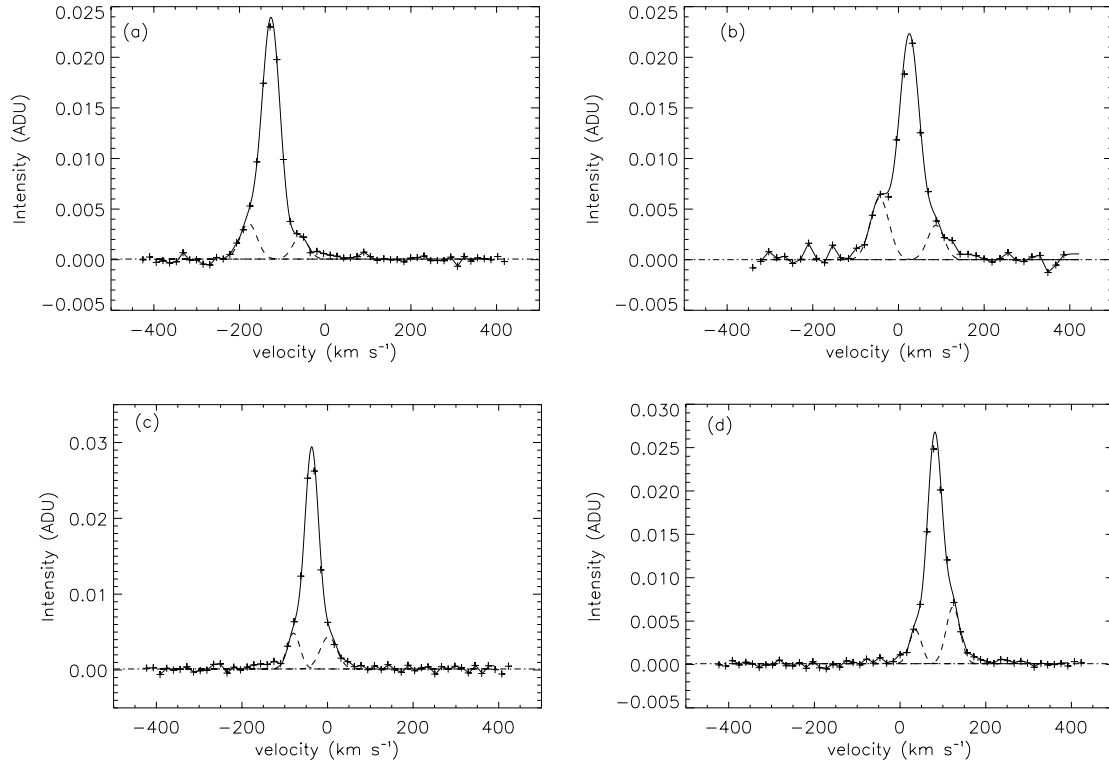


**Fig. 1.** Examples of H II region line profiles showing *wing* features. In dashed line we show the red and blue Gaussian components fitted to the observed spectrum, the continuous line show the result of the fit as a sum of the Gaussian components fitted to the spectrum.

square noise level of the line profiles<sup>2</sup>. This last criterion ensures that a single wing feature can not be confused with noise.

Down to a limit of  $\log L_{\text{H}\alpha} = 38.0$  ( $\text{erg s}^{-1}$ ), the H II regions whose line profiles show wing features satisfying the criteria defined above represent for NGC 3359, NGC 6951 and NGC 1530 respectively, 26.77%, 42.0% and 31.63% of the total number of identified H II regions for each galaxy. The fraction of the spectra classified as 1 P+2 W or 1 P+1 W, (where P and W stand for central peak and wing component, respectively) satisfying the criteria are: 48.75% for NGC 3359, 60.0% for NGC 6951 and 81.58% for NGC 1530. The differences between these last three fractions are due to the S:N of the line profiles for each galaxy, which have mean values at the line centres of 29.3 for NGC 3359, 41.8 for NGC 6951 and 51 for NGC 1530. The galaxy with the highest S:N has a higher fraction of H II regions with line profiles having secondary Gaussian components satisfying the criteria shown above. The increase in the fraction of detectable components with S:N ratio leads us to predict that at a sufficiently high value of S:N most, if not all, H II regions would show these wing features.

For the sample of H II regions selected, we obtained line profiles with increasing apertures; starting from a line of sight through the centre of the region (line spectrum taken with an aperture of  $1 \times 1$  pixel), we continued opening the aperture till we covered the whole emitting area of the region and analyzed each spectrum using Gaussian functions. We obtained a sample of isolated H II regions, whose line profiles show wing

features in more than one, and usually all of the line profiles of the set obtained with different apertures. With this procedure we guarantee that the secondary components of the final selected sample of line profiles show the emission from the given region, and that they are not contaminated by the emission of neighbouring regions.

With these considerations, we obtain a sample of 14, 13 and 19 isolated H II regions for NGC 1530, NGC 6951 and NGC 3359, respectively, with clearly defined wing features in their set of line profiles. We finally added 4 regions for NGC 1530 and NGC 6951 and 2 for NGC 3359, which were not completely isolated but show clearly defined wings in the set of line profiles.

### 2.3. Selection of the best line profile for each H II region

In order to obtain the parameters of the wings for each H II region, we have selected from the set of line profiles with different apertures that which best defines the wing features. This is the one with the highest mean S:N for the two secondary components. In Tables 1–3 we show the aperture for the best line profile selected for each H II region in the three galaxies, as well as the mean S:N ratio, the parameters for the red and blueshifted components, the Emission Measure ( $EM$ )<sup>3</sup> of the shifted components as a fraction of the total Emission Measure

<sup>2</sup> The line profiles show a S:N $\sim$ 40, thus the criterion we applied for single wings implies that their amplitudes must be at least  $\sim$ 10% of the amplitude of the central peak.

<sup>3</sup> The value of the Emission Measure is taken as proportional to the integrated area of the relevant fitted Gaussian component, so that the total Emission Measure for the H II region will be proportional to the integrated area of the complete line profile.

**Table 1.** Parameters of the wing features of the selected line profile that best defines the wing components from the set of spectra taken with different apertures for each H II region in NGC 1530. Column 1: H II region number from the catalogue (Relaño et al. 2004). Column 2: logarithmic  $H\alpha$  luminosity taken from the catalogue. Column 3: aperture of the selected line profile. The pixel size is  $0.29''$ , which gives a pixel scale of  $51.4 \text{ pc/pix}$  at a galaxy distance of  $36.6 \text{ Mpc}$  (Tully 1988). Column 4: mean S:N of both wing components. Column 5: emission measure of the red component as a fraction of the total  $EM$  of the region. Column 6: standard deviation of the fractional emission measures of the red Gaussian components fitted to the set of line profiles with different apertures taken for each H II region. Columns 7 and 8: equivalent parameters to those defined in Cols. 5 and 6 but for the blue wing components. Column 9: velocity separation between the central peak and the red wing component. Column 10: standard deviation of the quantities in Col. 9 for the set of line profiles with different apertures extracted for each H II region. Columns 11 and 12: equivalent parameters defined respectively in Cols. 9 and 10 but for the blue wing component. Notes: region 70 is included in the sample because its red wing component has  $\Delta v_r > 46.55 \text{ km s}^{-1}$  and region 73 is considered to satisfy the criterion selection that its wing must have a velocity separation bigger than 2.5 times the spectral resolution of the data cube ( $46.55 \text{ km s}^{-1}$ ), if the estimated error for  $\Delta v_r$  is considered.

Region (number)	$\log L_{H\alpha}$ ( $\text{erg s}^{-1}$ )	Aperture $\text{pc} \times \text{pc}$	S:N	$EM_r$ (%)	Stdev. (of $EM_r$ )	$EM_b$ (%)	Stdev. (of $EM_b$ )	$\Delta v_r$ ( $\text{km s}^{-1}$ )	Stdev. (of $\Delta v_r$ )	$\Delta v_b$ ( $\text{km s}^{-1}$ )	Stdev. (of $\Delta v_b$ )
2	39.71	$155 \times 155$	8.66	7.88	0.92	4.80	1.44	56.17	0.64	67.35	0.68
6	39.64	$257 \times 257$	13.72	8.21	1.56	9.40	0.92	87.60	8.07	78.60	4.95
7	39.59	$361 \times 361$	17.70	12.86	1.98	8.61	0.99	66.59	2.53	75.62	2.19
8	39.45	$257 \times 257$	10.11	7.09	0.65	9.65	2.22	73.74	1.11	55.71	3.27
9	39.42	$154 \times 154$	13.07	6.61	1.17	7.75	2.00	72.27	2.38	83.79	7.68
10	39.42	$257 \times 257$	15.88	8.33	1.16	11.44	0.97	69.75	2.46	72.68	3.49
12	39.43	$154 \times 154$	11.12	8.53	1.01	7.48	2.44	96.23	11.79	87.59	5.91
14	39.34	$257 \times 257$	12.44	7.87	0.83	6.16	0.95	87.72	6.04	67.56	1.49
22	39.12	$257 \times 257$	5.27	6.55	1.52	7.98	0.68	49.30	7.24	49.46	15.25
27	39.05	$257 \times 257$	11.59	14.74	3.40	3.78	1.48	61.38	12.85	77.95	4.43
33	38.86	$154 \times 154$	8.79	6.73	2.07	24.67	9.73	54.48	7.62	53.48	6.76
41	38.84	$263 \times 263$	6.93	8.79	1.81	17.89	2.18	61.78	1.44	69.38	1.80
70	38.50	$154 \times 154$	4.60	5.09	1.45	12.58	2.38	63.69	2.25	44.67	1.22
73	38.42	$154 \times 154$	12.13	15.85	5.61	0.00	0.00	44.96	3.12	0.00	0.00
81	38.36	$257 \times 257$	4.59	9.30	0.05	4.75	0.28	85.49	7.19	78.05	2.88
84	38.39	$154 \times 154$	7.05	0.00	0.00	16.15	3.19	0.00	0.00	47.84	5.40
92	38.29	$257 \times 257$	3.72	10.37	1.26	7.97	0.12	79.32	6.22	78.95	2.74
103	38.09	$154 \times 154$	5.07	20.71	4.56	0.00	0.00	54.75	2.12	0.00	0.00

of the region and the velocity separation between the wing features and the central component.

It is interesting to note that the parameters of the high velocity components do not change significantly in the set of line profiles taken with different apertures for the same H II region. This can be seen from the standard deviation values of each wing parameter shown in Tables 1–3, which are the standard deviations obtained from the values of these quantities for the spectra with different apertures, excluding the  $1 \times 1$  spectrum<sup>4</sup>. Thus, we take the fit parameters of the best S:N line profile as the characteristic values of the wing features for each H II region.

#### 2.4. Verifying the existence of the high velocity features

The shape of the recorded spectral line is broadened by the TAURUS-II interferometer instrument function, which shows low level extended non-Gaussian tails extending over  $100 \text{ km s}^{-1}$  from the centre of its most intense peak to the blue and the red, as it can be seen in Fig. 2. These instrumental

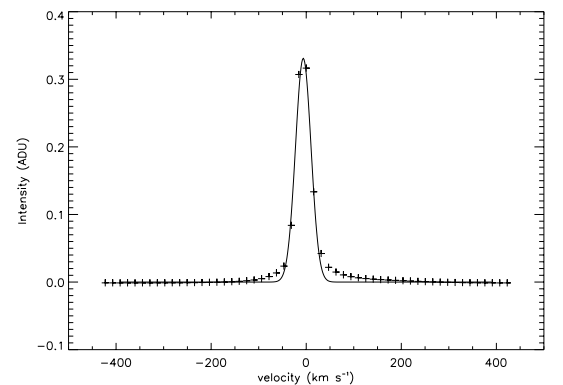


**Fig. 2.** Normalized instrumental response of the Fabry-Pérot TAURUS-II obtained from the calibration lamp used in the observations of NGC 3359, shown as an example of Lorentzian instrument response function. The instrumental response function extracted from the calibration data cubes corresponding to the observations of NGC 6951 and NGC 1530 are similar to that one shown here for NGC 3359.

components affect the high velocity, low intensity features detected in the spectra of the H II regions. In order to study further the physical implications of the high velocity components, we verified that they are not due to the response function

<sup>4</sup> We do not use the spectra with a  $1 \times 1$  pixel aperture because this aperture is below the limit of the angular resolution for all the three galaxies.

**Table 2.** The same parameters as in Table 1 for the H II region line profiles of NGC 6951. For a pizel size of 0.58'' the pixel scale is 67.8 pc/pix at a distance galaxy of 24.1 Mpc (Tully 1988). Notes: regions 24 and 27 have a single fitted spectrum (apart from the spectrum  $1 \times 1$ ) of the set of the line profiles extracted with different apertures for each region. The parameters for the wings are those for the single fitted spectrum. Since we have only a single value for each parameter we could not obtain the corresponding standard deviation. The red wing feature of region 36 has a velocity separation less than 2.5 times the spectral resolution of the data cube ( $39.08 \text{ km s}^{-1}$ ), we include it in the sample since the blue wing does satisfy the criterion.

Region (number)	$\log L_{\text{H}\alpha}$ ( $\text{erg s}^{-1}$ )	Aperture (pc $\times$ pc)	S:N	$EM_r$ (%)	Stdev. (of $EM_r$ )	$EM_b$ (%)	Stdev. (of $EM_b$ )	$\Delta v_r$ ( $\text{km s}^{-1}$ )	Stdev. (of $\Delta v_r$ )	$\Delta v_b$ ( $\text{km s}^{-1}$ )	Stdev. (of $\Delta v_b$ )
2	39.27	339 $\times$ 339	17.76	6.36	1.14	11.09	0.29	69.88	3.91	51.98	0.69
4	39.11	203 $\times$ 203	10.54	8.55	1.05	8.61	1.80	56.89	0.25	47.28	4.73
6	38.97	203 $\times$ 203	8.96	10.72	0.50	12.34	0.72	48.40	1.10	45.79	1.34
10	38.84	339 $\times$ 339	13.10	8.81	2.20	12.76	5.27	39.10	0.59	44.35	4.41
11	38.82	203 $\times$ 203	10.09	6.38	0.80	11.22	1.75	68.37	3.85	52.57	3.18
12	38.81	339 $\times$ 339	4.95	10.10	0.43	6.10	1.29	67.80	1.96	63.02	1.27
13	38.80	203 $\times$ 203	10.43	11.85	1.69	6.28	0.30	43.51	1.62	50.91	1.38
15	38.74	203 $\times$ 203	3.39	5.28	0.55	2.58	0.29	83.23	11.13	69.49	2.23
18	38.67	339 $\times$ 339	7.04	3.52	1.69	9.10	1.07	49.83	4.05	45.41	1.12
24	38.52	203 $\times$ 203	7.59	6.92	==	9.45	==	54.83	==	47.06	==
27	38.45	339 $\times$ 339	4.73	0.00	0.00	9.74	==	0.00	0.00	48.45	==
36	38.37	339 $\times$ 339	7.72	10.08	1.29	11.39	2.69	36.40	1.75	40.84	0.61
41	38.35	203 $\times$ 203	7.08	14.28	3.42	10.69	0.69	43.88	7.73	57.75	4.62
62	38.17	203 $\times$ 203	2.93	10.08	2.05	5.52	1.44	83.50	13.04	84.73	13.99
67	38.13	203 $\times$ 203	7.58	9.81	1.31	12.24	3.94	45.21	4.09	40.45	5.14
69	38.11	339 $\times$ 339	4.13	7.95	1.29	0.00	0.00	78.53	0.00	0.00	0.00
75	38.06	339 $\times$ 339	4.19	12.42	4.19	0.00	0.00	51.53	4.28	0.00	0.00

of TAURUS-II. To do this, we deconvolved a set of characteristic observed line profiles using the method devised by Lucy (1974), which allows the deconvolution of frequency distributions with a finite sample size.

This method is based on the fact that an exact reproduction of the observed function is not required since this distribution has its own statistical fluctuations. Thus, any solution of the deconvolved function for which the corresponding convolved function is close enough to the observed profile for the differences to be ascribable to sampling errors, is a possible solution. The iterative estimation procedure applied to this problem is that of minimizing  $\chi^2$ , which is a measure of the goodness of the fit to the data, keeping normalization and non-negativeness of the solution conserved.

Figure 3 shows the output from an application of the Lucy algorithm to two H II regions: region 41 of NGC 1530 and region 6 of NGC 3359. The normalized observed spectrum and the result of its fit is shown with a continuous line in these figures. The dashed line shows the result of the fit to the deconvolved spectrum obtained using Lucy's method and the dashed-dot line shows the fit of the blue and redshifted components to the deconvolved function. The iterative procedure to obtain the deconvolved function was stopped at the iteration that produces a central component in the deconvolved function with a velocity dispersion close to the value obtained by the subtraction in quadrature of the observed and the instrumental velocity dispersions. Thus, the deconvolution of the central

(and most intense) peak is guaranteed<sup>5</sup>. In Table 4 we show the fit parameters for the observed and deconvolved spectra for the H II regions in Fig. 3. For high velocity features which do not have a high S:N and are close to the central most intense peak, the result of the application of Lucy's method for deconvolution is to bring them nearer to the centre of the main Gaussian component and to reduce their integrated areas (see parameters of the wing components of region 6 and the red component of region 41 in Table 4). When the high velocity features have high S:N and is clearly separated from the central component, the deconvolved spectra shows the shifted component located at a similar velocity and with similar integrated area to the observed line profile.

The results obtained for the deconvolution of these two line profiles show that the observed wings are not artefacts of the response function of TAURUS-II, because the deconvolution of the observed line using the instrument profile shows not only the central peak but also clearly reveals the high velocity features.

However, Lucy's method is difficult to use to extract the physical parameters of the shifted components because the criterion for optimizing the number of iterations is too sensitive to the noise level of the spectrum and to the intensity peak of the component: the S:N ratio is varying too rapidly across the line

<sup>5</sup>  $\sigma_{\text{dec}(\text{cent})} = 16.8 \pm 0.6 \text{ km s}^{-1}$  for reg. 41 and  $\sigma_{\text{dec}(\text{cent})} = 17.9 \pm 0.3 \text{ km s}^{-1}$  for reg. 6.

**Table 3.** Parameters of the wing features of the selected line profile that best defines the wing components from the set of spectra taken with different apertures for each H II region in NGC 3359. The columns have the same meaning as those in Table 1. For a pixel size of  $0.56''$  the pixel scale is  $36.4$  pc/pix at a galaxy distance of  $13.4$  Mpc (de Vaucouleurs et al. 1991). Notes: regions 140 and 192 have a single fitted spectrum of the set of line profiles extracted with different apertures for each region. The parameters for the wings are those for the single fitted spectrum. Region 56 was kept in the sample although the velocity separation for its red component is not bigger than 2.5 times the spectral resolution of the data cube ( $41.65$  km s $^{-1}$ ). The red components of regions 19 and 42 and the blue components of regions 42 and 83 satisfy the criterion if the estimated errors for  $\Delta v_r$  are taken into account.

Region (number)	$\log L_{H\alpha}$ (erg s $^{-1}$ )	Aperture (pc $\times$ pc)	S:N	$EM_r$ (%)	Stdev. (of $EM_r$ )	$EM_b$ (%)	Stdev. (of $EM_b$ )	$\Delta v_r$ (km s $^{-1}$ )	Stdev. (of $\Delta v_r$ )	$\Delta v_b$ (km s $^{-1}$ )	Stdev. (of $\Delta v_b$ )
1	39.57	182 $\times$ 182	18.61	8.06	0.55	6.95	0.85	63.16	0.92	64.10	6.17
6	39.15	109 $\times$ 109	10.78	8.11	1.28	5.87	0.86	61.94	5.44	65.99	2.89
15	38.98	109 $\times$ 109	6.07	1.69	0.77	2.04	0.85	82.04	2.30	81.78	2.02
16	38.94	109 $\times$ 109	4.37	1.73	0.40	1.55	0.48	83.87	2.86	85.25	2.62
17	38.92	109 $\times$ 109	6.17	9.39	1.52	3.04	0.60	52.48	6.00	82.12	2.61
19	38.91	182 $\times$ 182	24.70	13.62	0.98	17.44	0.67	41.50	2.39	42.20	0.52
38	38.63	109 $\times$ 109	11.35	0.00	0.00	10.55	2.73	0.00	0.00	45.96	1.44
42	38.58	109 $\times$ 109	11.51	13.23	4.17	11.34	2.77	41.13	2.80	40.70	2.41
44	38.57	109 $\times$ 109	6.68	3.77	3.45	2.74	0.65	68.24	3.88	50.10	2.42
45	38.55	109 $\times$ 109	16.54	17.02	3.76	8.85	1.81	42.47	1.49	45.15	5.27
47	38.54	109 $\times$ 109	4.81	4.39	0.64	3.02	0.13	70.83	1.54	83.74	0.68
51	38.52	109 $\times$ 109	9.37	10.72	0.23	11.14	0.28	44.41	1.63	49.04	0.94
52	38.51	109 $\times$ 109	9.49	7.98	0.42	7.96	0.19	46.55	0.55	43.40	2.13
53	38.49	109 $\times$ 109	4.74	4.11	0.27	1.94	0.45	63.46	0.79	58.65	5.24
56	38.46	109 $\times$ 109	9.86	17.08	2.60	5.51	0.61	37.68	1.44	51.28	0.93
83	38.25	109 $\times$ 109	13.23	11.00	0.61	15.62	0.46	41.86	0.54	40.52	1.03
92	38.19	109 $\times$ 109	6.57	3.84	0.99	7.77	0.96	58.70	1.07	45.26	2.07
103	38.12	109 $\times$ 109	4.46	6.31	0.46	0.00	0.00	55.86	1.47	0.000	0.00
140	37.94	109 $\times$ 109	4.54	0.00	0.00	18.79	==	0.00	0.00	51.17	==
155	37.88	109 $\times$ 109	3.42	7.34	2.59	4.63	0.13	47.03	3.51	52.19	0.92
192	37.73	109 $\times$ 109	2.63	5.30	==	6.51	==	57.46	==	52.85	==

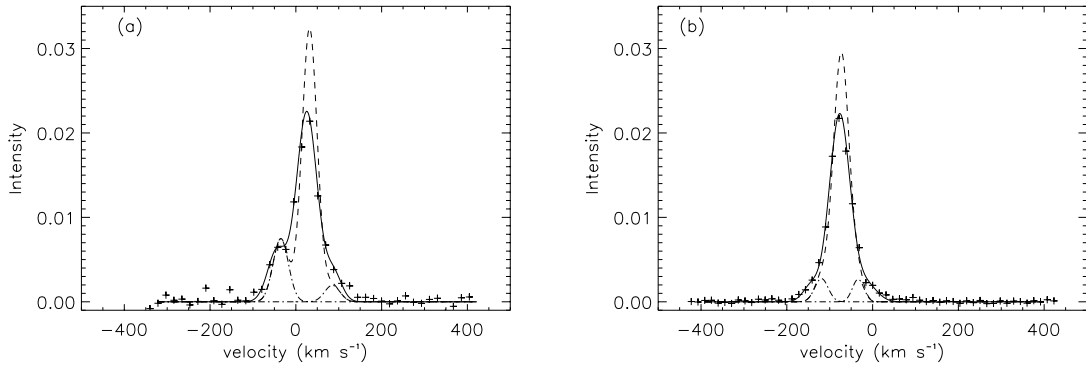


**Fig. 3.** Deconvolution of the line profiles for **a)** region 41 of NGC 1530 and **b)** region 6 of NGC 3359. The points show the observed profile and the continuous line represents the result of the fit to the observed data. The dashed line is the result of the fit of the deconvolved function obtained using Lucy's method and the dashed-dot line shows the low intensity components of the fitted deconvolved spectrum.

profile to give fully consistent values for strong and weak features. For these reasons the deconvolution with Lucy's method cannot be used systematically where quantitative inferences are required, but could be reliably used to verify the existence of the high velocity features.

### 3. Observational parameters of the wing features

We have studied the wing features through their fit parameters: area, centre and widths of the fitted Gaussian components. The

relation between the Emission Measure, velocity and velocity dispersion of the wing features for the best S:N line profile and the logarithmic  $H\alpha$  luminosity for the H II regions in Tables 1–3 are shown in Figs. 4–6. There are two ways to determine the errors involved in the fit parameters: first, the measured variation of the parameters in the set of line profiles taken with different apertures for each H II region and second the estimated error of the parameter given by the fit program. In all the figures we show in this section we have plotted the error bars corresponding to the first method of error estimation mentioned above.

**Table 4.** Parameters of the Gaussian components fitted to the observed and deconvolved spectra of the H II regions 41 of NGC 1530 and 6 of NGC 3359.  $v_c$ ,  $v_r$  and  $v_b$  are the peak velocities of the central, red and blue component, these velocities are referred to the systemic velocity of the galaxy,  $v_{\text{sys}}(\text{NGC 1530}) = (2466 \pm 4) \text{ km s}^{-1}$  (Zurita et al. 2003) and  $v_{\text{sys}}(\text{NGC 3359}) = (1006.8 \pm 0.3) \text{ km s}^{-1}$  (Rozas et al. 2000b).  $\sigma_c$ ,  $\sigma_r$  and  $\sigma_b$  are the velocity dispersions of the central, red and blue component, respectively.

Region 41	$v_c$	$v_r$	$v_b$	$\sigma_c$	$\sigma_r$	$\sigma_b$	$EM_r$	$EM_b$
Observed	$25.5 \pm 2.0$	$87.3 \pm 13.3$	$-43.9 \pm 7.1$	$24.2 \pm 3.4$	$19.2 \pm 13.3$	$21.9 \pm 6.6$	8.8%	17.9%
Deconvolved	$32.0 \pm 1.0$	$85.0 \pm 16.0$	$-35.2 \pm 2.8$	$17.7 \pm 1.0$	$17.8 \pm 16.7$	$18.0 \pm 3.0$	4.7%	18.1%
Region 6	$v_c$	$v_r$	$v_b$	$\sigma_c$	$\sigma_r$	$\sigma_b$	$EM_r$	$EM_b$
Observed	$-76.7 \pm 0.8$	$-14.8 \pm 10.3$	$-142.7 \pm 5.9$	$24.2 \pm 1.1$	$24.7 \pm 6.3$	$19.1 \pm 5.1$	8.1%	5.9%
Deconvolved	$-73.0 \pm 0.5$	$-33.7 \pm 5.1$	$-119.3 \pm 5.3$	$18.5 \pm 1.0$	$13.4 \pm 2.7$	$15.6 \pm 3.5$	6.9%	5.7%

We have also obtained for comparison, the mean error of the corresponding parameter given by the fit program. For the three parameters: area, centre and width, the errors given by the fit program are bigger than the standard deviations of the values obtained for different apertures. For the centre of the Gaussian, the errors from the fit are  $\sim 8 \text{ km s}^{-1}$ , which is half of the spectral resolution of the observed Fabry-Pérot data cube, while the standard deviation of the centre of the Gaussian fitted to the spectra with different apertures is  $\sim 3 \text{ km s}^{-1}$ . This means two things: first, the variation of the parameters for different apertures is small, which allows us to take as a canonical observational parameter that obtained from the fit of the best S:N line profile and, second, the S:N ratios are high enough to allow us to resolve features with a better resolution than the nominal spectral resolution of the data cubes, given by the separation between planes of the data cube.

### 3.1. Emission Measure versus $\log L_{H\alpha}$

The fractional Emission Measure of the wing features obtained as the ratio between the wing area and the total area of the line profile versus the logarithmic  $H\alpha$  luminosity is shown in Fig. 4a for the red wing and Fig. 4b for the blue wing, respectively. The mean value for the fractional Emission Measures of red and blue components is 8.9% in both cases. In Figs. 4 we also show, with a dashed line the corresponding linear fits to the data in the plots. The linear correlation coefficients show that there is no apparent relation between the fractional Emission Measures and the logarithmic  $H\alpha$  luminosity;  $r_{\text{red}} = -0.1405$  and  $r_{\text{blue}} = -0.1007$ .

### 3.2. Velocities versus $\log L_{H\alpha}$

In Figs. 5 we show the velocity separation between the shifted and most intense, i.e. the central, Gaussian components of the best S:N line profiles versus the logarithmic  $H\alpha$  luminosity. Figures 5a and b show respectively the velocity separation of the red and blue component with respect to the central peak,  $v_{\text{red}}$  ( $v_{\text{blue}}$ ), versus  $\log L_{H\alpha}$ . The two plots are quite similar, showing the symmetry of the shifted components with respect to the central and most intense component. The velocity separations range from  $40 \text{ km s}^{-1}$  to  $90 \text{ km s}^{-1}$  for these luminous H II regions. The mean value for the velocity separation is

$\langle v_{\text{red}} \rangle = 60.5 \text{ km s}^{-1}$  and  $\langle v_{\text{blue}} \rangle = 59.02 \text{ km s}^{-1}$ . There is a slight trend of increasing velocity separation with increasing  $\log L_{H\alpha}$ , which can be seen in the linear fits plotted in dashed lines for each parameter with linear correlation coefficients  $r_{\text{red}} = 0.3417$  and  $r_{\text{blue}} = 0.4038$ .

### 3.3. Wing feature velocity dispersions versus $\log L_{H\alpha}$

The relation between the velocity dispersion of the wing features for the selected H II regions and the logarithmic  $H\alpha$  luminosity is shown in Fig. 6. The red velocity dispersion is slightly higher than the blue one, as can be seen from comparison of Figs. 6a and b and from the mean values  $\langle \sigma_{\text{red}} \rangle = 19.5 \text{ km s}^{-1}$  and  $\langle \sigma_{\text{blue}} \rangle = 17.0 \text{ km s}^{-1}$ . As can be seen from the figures, the wing velocity dispersions are low, in some cases below the corresponding instrumental velocity dispersion. This means that in general the features are not well resolved, but the fact that the selected features satisfy the selection criteria explained in Sect. 2.2 imply that they are well detected and that, although their velocity dispersions are not reliable values, their velocity separations and Emission Measures can be used to extract physical information from the features.

### 3.4. Velocity dispersion of the central component versus $\log L_{H\alpha}$

Figure 7a shows the observed velocity dispersion for the central Gaussian component versus the logarithmic  $H\alpha$  luminosity. There is a clear trend of increasing observed velocity dispersion with increasing logarithmic  $H\alpha$  luminosity, which can be seen from the linear fit to the data points in this plot. The mean value of the observed velocity dispersion for all the H II regions is  $23.5 \text{ km s}^{-1}$ . The trend of increasing  $\sigma$  with increasing  $\log L_{H\alpha}$  is also maintained for the *deconvolved*<sup>6</sup> velocity dispersion, as can be seen in Fig. 7b. However, there are some H II regions in this plot with significantly low values of the deconvolved velocity dispersions for their central components. These H II regions show in their line profiles wing features with high fractional Emission Measures and located relatively close in velocity to the central most intense component.

<sup>6</sup>  $\sigma_{\text{deconv}} = (\sigma_{\text{obs}}^2 - \sigma_{\text{inst}}^2)^{1/2}$ , where  $\sigma_{\text{inst}}$  is the instrumental velocity dispersion of the data cube of each galaxy.

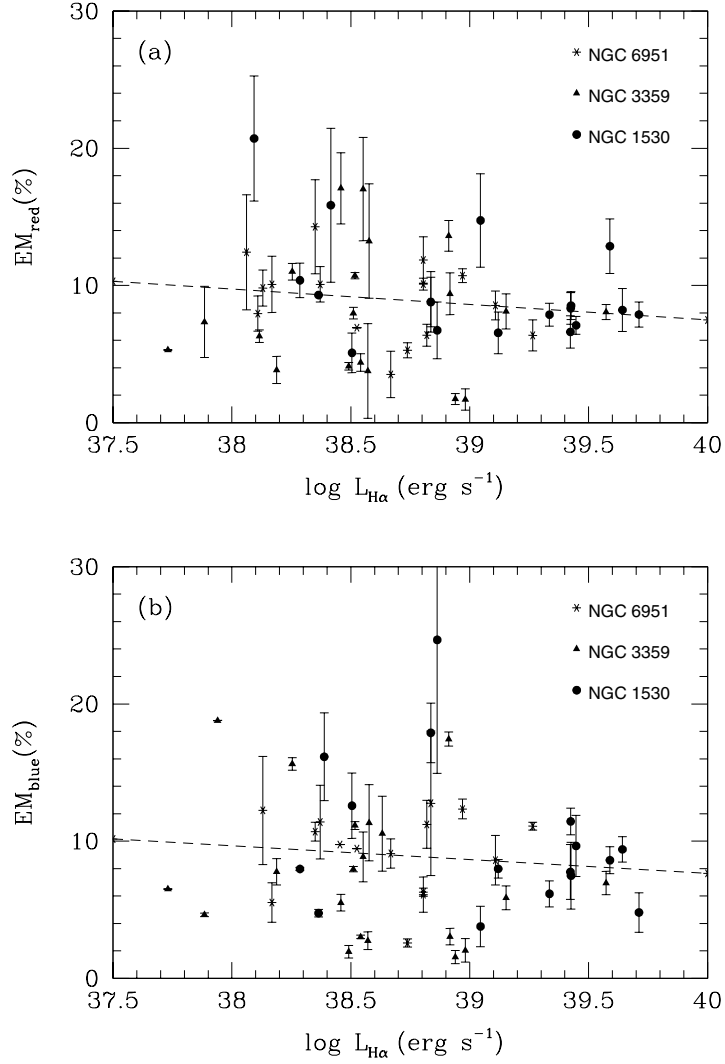


**Fig. 4.** **a)** Emission Measure for the red shifted Gaussian components fitted to the best S:N spectra of the selected H II regions shown in Tables 1–3 versus  $\log L_{H\alpha}$  of the H II region. The Emission Measure is given as a fraction of the total  $EM$  of the region. **b)** Emission Measure of the blue shifted Gaussian component versus  $\log L_{H\alpha}$  for the same H II regions as in plot **a)**. The points without plotted error bars are for regions where only a single sampling area was possible, so that no meaningful measure of scatter could be derived.

#### 4. Interpretation of the high velocity features

We interpret the wing features observed as signatures of supersonic expanding shells within the H II region. A line profile extracted for such an H II region would have a central high intensity component produced by the emission of the bulk of gas inside the region and high velocity, low intensity features symmetrically located with respect to the central peak produced by the emission of the shell. We use the observational parameters of these secondary components described in Sect. 3 to describe the properties of the shell and to quantify its energetics for each H II region of the selected sample.

##### 4.1. Shell electron density

For a completely ionized thin shell of radius  $R_{\text{shell}}$  and thickness  $\Delta R$ , the  $H\alpha$  luminosity of the shell will be:

$$L_{H\alpha}(\text{shell}) = 4\pi R_{\text{shell}}^2 \Delta R n_{\text{shell}}^2 \alpha_{H\alpha}^{\text{eff}}(H, T) h\nu_{H\alpha} \quad (1)$$

where  $\alpha_{H\alpha}^{\text{eff}}(H, T)$  is the effective recombination coefficient in the  $H\alpha$  emission line. From Eq. (1), we can obtain the shell electron density  $n_{\text{shell}}$ , using the following considerations. For each H II region, we obtain the  $H\alpha$  luminosity of the shell multiplying the total  $H\alpha$  luminosity of the region given by our catalogue by the fractional area that the wings show in the best S:N line profile with respect to the total area of the line profile. We make a basic zero order assumption for the shell radius of  $R_{\text{shell}} = 0.2 R_{\text{reg}}$ , where  $R_{\text{reg}}$  is the H II region radius, and a thickness of  $\Delta R = 4.5$  pc. These values are estimates from the values of the most luminous expanding shells detected in 30 Doradus by Chu & Kenicutt (1994) and NGC 604 by Yang et al. (1996). We cannot test the possibility that there are shells with larger radii or larger thicknesses; since it is not possible to obtain directly values of these parameters for H II regions at the distances of the galaxies observed here. We have therefore used the values derived for nearby extragalactic H II regions with similar  $H\alpha$  luminosities to those of the regions of our sample, which are among the most luminous regions found.



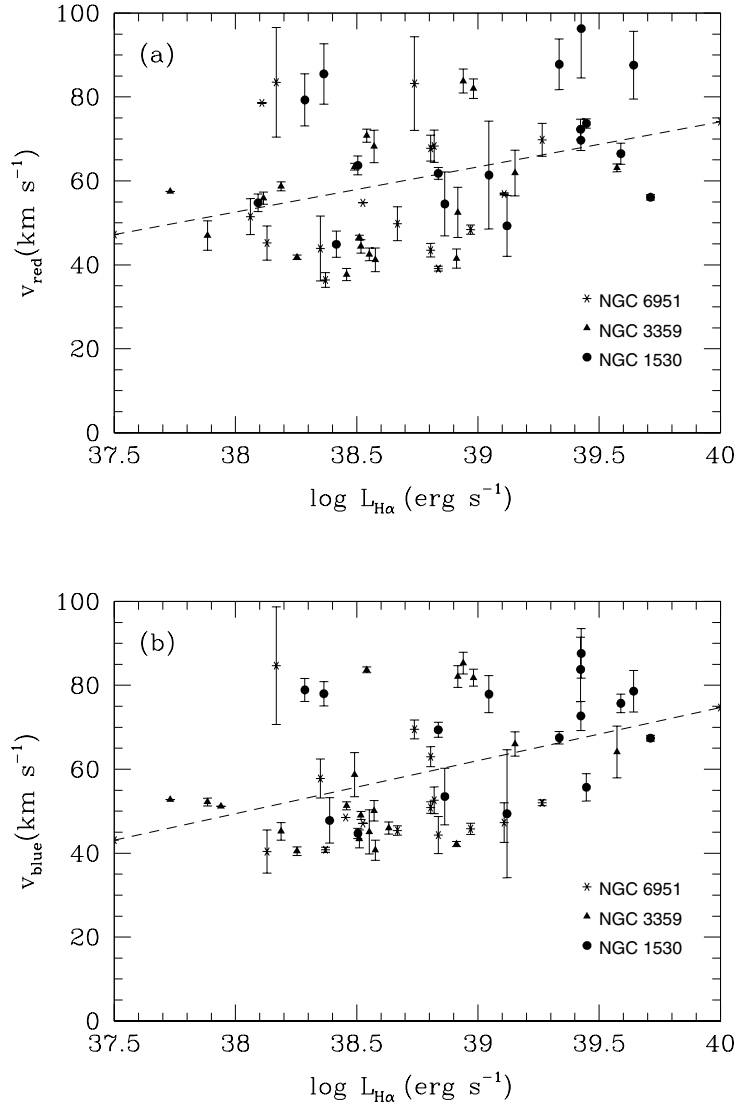


**Fig. 5. a)** Velocity separation between the red shifted component and the central and most intense component fitted to the best S:N spectrum of the selected H II regions in NGC 1530, NGC 6951 and NGC 3359 versus  $\log L_{\text{H}\alpha}$  of the H II region. **b)** The same plot as in **a)** but for the blue shifted component. For an explanation of the points with no plotted error bars see Figs. 4.

The values of the shell densities for the H II region sample of NGC 1530, NGC 3359 and NGC 6951 are shown in Col. 4 of Tables 5–7. The mean values of  $n_{\text{shell}}$  for the galaxies are 11.5 cm $^{-3}$ , 6.4 cm $^{-3}$  and 8.2 cm $^{-3}$  for NGC 1530, NGC 3359 and NGC 6951, respectively.

#### 4.2. Energetics of the shell

The shell expansion velocities are taken as the mean values between the velocity separations of the red and blue components with respect to the central peak in each H II region. The values are shown in Col. 3 of Tables 5–7. The adopted shell radius in parsecs ( $R_{\text{shell}} = 0.2 R_{\text{reg}}$ ) for each H II region is shown in Col. 2 of the same tables. Using the value of the shell electron density for each H II region, we obtain the ionized mass of a thin shell integrating over its volume, thus:

$$M_{\text{shell}}(\text{H}^+) = 4\pi R_{\text{shell}}^2 \times \Delta R \times n_{\text{shell}} \times m_p \quad (2)$$

where  $m_p$  is the mass of the hydrogen atom. The mass of the shell is shown in Col. 5, the values are of order  $10^4 M_{\odot}$  and represent 18.9%, 26.2% and 24.2% of the total ionized mass of the region for NGC 1530, NGC 3359 and NGC 6951 respectively. In Col. 7 is shown the kinetic energy of the shell, obtained using the formula  $E_k = \frac{1}{2} m_{\text{shell}} v_{\text{shell}}^2$ . The energies are of order  $\sim 10^{51}$  erg, which is the same order as the kinetic energies of the most luminous shells in 30 Doradus and NGC 604.

We have compared the kinetic energy of the shell with input energies from the central stars. We use the observed H $\alpha$  luminosity of the region to derive an equivalent number of O3(V) type stars (Col. 6 of Tables 5–7), using the H $\alpha$  luminosity for an O3(V) type star given by Vacca et al. (1996). We will see that for models based on stellar winds as the principal source of shell kinetic energy, the method gives only lower limit estimates of the input energy for two reasons: first, we do not take into account the photon escape fraction for the H II regions, that can be as high as  $\sim 80\%$  of the ionizing

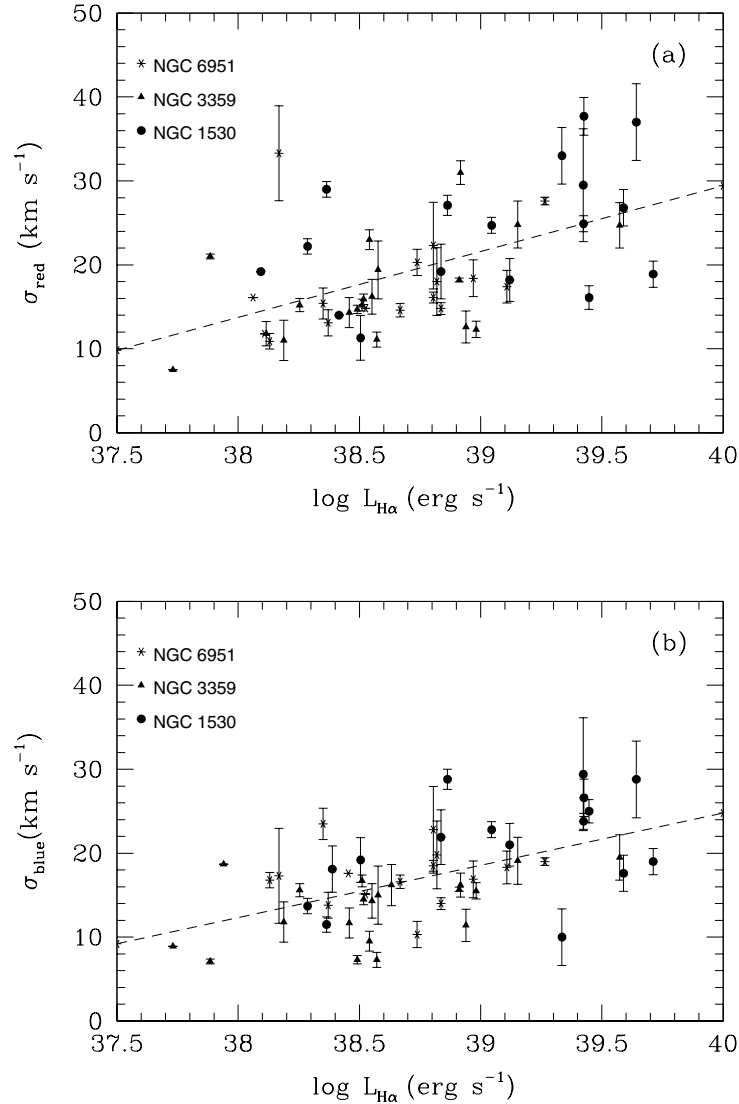


**Fig. 6.** Observed velocity dispersion for the red **a)** and blue **b)** shifted component fitted to the best S:N spectrum of the selected H II regions in NGC 1530, NGC 6951 and NGC 3359 versus  $\log L_{\text{H}\alpha}$  of the H II region. For an explanation of the points with no plotted error bars see Figs. 4.

radiation for the most luminous H II regions (see Zurita 2001), and second, new recent effective temperatures for O(V) type stars would imply a reduction of the total logarithmic luminosity of these stars of  $\sim 0.1$  (Martins et al. 2002), larger equivalent number of O3(V) type stars obtained from the observed  $\text{H}\alpha$  luminosity would imply higher energy inputs than those shown in Tables 5–7.

Assuming a mean lifetime of  $10^6$  yr for the central ionizing stars, we can estimate their integrated wind energies, using the wind luminosity for an O3(V) spectral type star,  $\log L_{\text{wind}} = 37.08$  ( $\text{erg s}^{-1}$ ), given by Leitherer (1998). The values are shown in Col. 8 of Tables 5–7.

For comparison with the wind energy input, we show in Col. 10 the energy of the ionizing radiation, obtained using the number of Lyman continuum ionizing photons ( $7.4 \times 10^{49}$   $\text{photon s}^{-1}$ ) for an O3(V) type star given by Vacca et al. (1996). Although recent studies by Martins et al. (2002) give somewhat lower values than these earlier studies, the overall energy budget for the ionizing radiation would in any case be

higher than that of the winds by at least two orders of magnitude. In Col. 11 we show a first order approximation to the total radiative energy input for the H II region assuming that the ionizing stars emit as blackbodies of temperature  $T_{\text{eff}} = 51\,230$  K and have a radius of  $R = 13.2 R_{\odot}$ , (Vacca et al. 1996).

In Col. 9 we show the turbulent kinetic energy of the H II region. This is obtained from the total mass of the H II region and the non-thermal velocity dispersion of the central and most intense component,  $E_{\text{turb}} = \frac{1}{2} M_{\text{reg}} \sigma_{\text{nt}}^2$ . The values range from  $10^{49}$ – $10^{52}$  erg. There are some H II regions whose central component is not completely resolved, which are marked as “==” in Col. 9 of Tables 5–7. These H II regions show high intensity wing features located close to the central peak, whose lower expansion velocities could imply that the shells are located at greater distances from the centre of the region and that they could have been braked as they expand within the H II region. Besides, the higher fractional Emission Measures of these features with respect to the fractional EM of other H II regions means that they have more fractional mass in their shells. Thus,

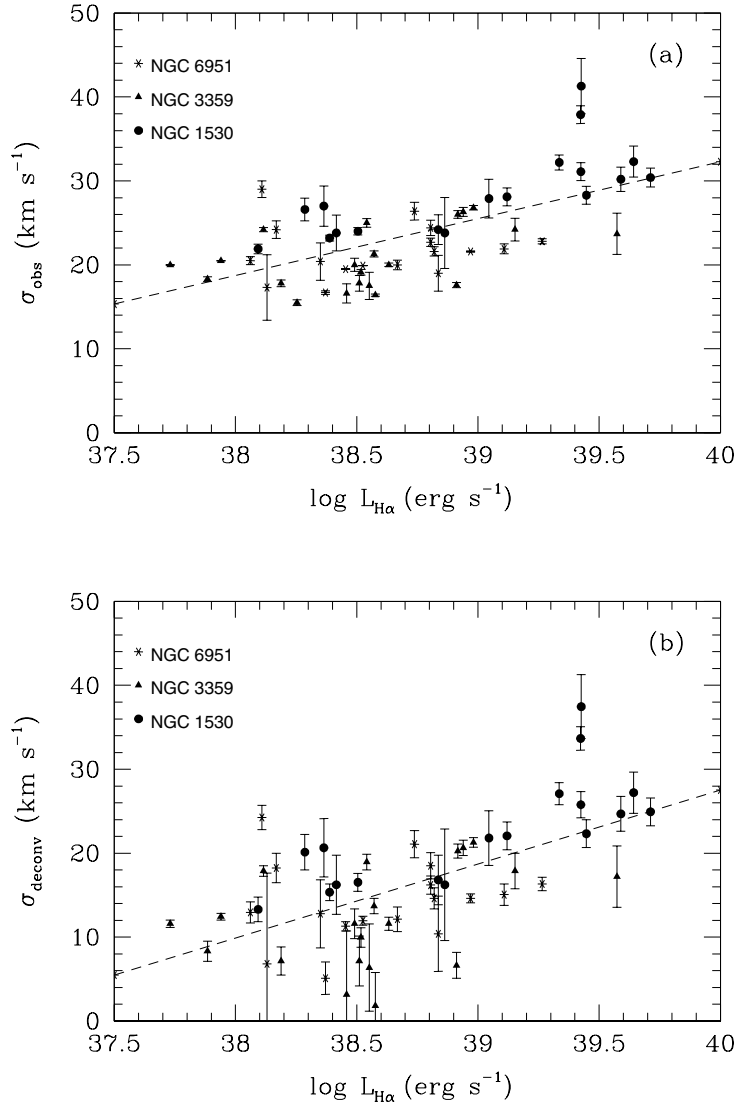


**Fig. 7.** Observed **a)** and deconvolved **b)** velocity dispersion for the central Gaussian component fitted to the best S:N spectrum of the selected H II regions in NGC 1530, NGC 6951 and NGC 3359 versus  $\log L_{H\alpha}$ . The error bar in **a)** correspond to the variation of the observed velocity dispersion for the set of line profiles taken for each H II region. The error bars in **b)** are estimated using the error bars in **a)** and the corresponding errors in the instrumental velocity dispersion for each galaxy.

the corresponding fractional masses inside the region will be lower and thus the turbulent components and velocity dispersions should also be lower, as we find in practice.

### 4.3. Discussion

The existence of an expanding shell in a significant fraction of H II regions might appear to be in contradiction with the results on nearby extragalactic H II regions where several shells with different radii have been observed. The contradiction is only apparent for two reasons:

1. Both studies, for 30 Doradus and NGC 604, show a specific expanding shell which is much brighter than the other shells detected in these regions and with similar radii in both cases,  $R_{shell} \sim 0.2 R_{reg}$ , and expansion velocities  $v_{exp} \sim 70$  km s $^{-1}$  for NGC 604 and  $v_{exp} \sim 40$  km s $^{-1}$  for

30 Doradus. The H $\alpha$  luminosity of the prominent shell in NGC 604 represents  $\sim 75\%$  of the total H $\alpha$  luminosity of the observed expanding shells. Besides, the integrated line profiles for these H II regions show extended wing features. In the case of 30 Doradus, Melnick et al. (1999) fitted the integrated line profile given by Chu & Kennicutt (1994) with two Gaussian components, the more intense and narrower central one and another much broader. Their widths (after correcting from thermal and instrumental broadening) are  $\sigma = 22$  km s $^{-1}$  and  $\sigma = 44$  km s $^{-1}$  for the narrow and broad one respectively. Melnick et al. (1999) interpreted this broad feature as a single turbulent motion of unknown origin. We interpret here this broadest Gaussian component as a shell with an expansion velocity of  $v_{exp} \sim 45$  km s $^{-1}$  moving inside the H II region as shown in a spectrum with either too low a velocity resolution or too low a S:N ratio to resolve the wing features. In fact, the line profile extracted

**Table 5.** Energetics of the shell and turbulent components of the sample of H II regions in NGC 1530. Column 1: H II region number from the catalogue. Column 2: shell radius. Column 3: measured shell expansion velocity. Column 4: mean shell electron density. Column 5: ionized mass of the shell. Column 6: equivalent number of O3(V) type stars. Column 7: kinetic energy of the shell. Column 8: combined kinetic energy of OB stellar winds, assuming an equivalent number of O3(V) type stars. Column 9: turbulent kinetic energy of the body of the H II region gas. Columns 10: combined energy of the ionizing radiation from the region OB stars. Column 11: combined total radiative energy of region OB stars emitting as black bodies.

Region (number)	$R_{\text{shell}}$ (pc)	$v_{\text{shell}}$ (km s <sup>-1</sup> )	$n_{\text{shell}}$ (cm <sup>-3</sup> )	$M_{\text{shell}}$ (10 <sup>4</sup> $M_{\odot}$ )	$N_{\text{eq}}$ (O3(V))	$E_{\text{K}}$ (10 <sup>51</sup> erg)	$E_{\text{wind(O3)}}$ (10 <sup>51</sup> erg)	$E_{\text{turb}}$ (10 <sup>51</sup> erg)	$E_{\text{rad}}$ (10 <sup>54</sup> erg)	$E_{\text{total,rad}}$ (10 <sup>54</sup> erg)
2	88.64	61.76	11.90	13.1	50.61	5.0	19.2	60.0	2.6	6.6
6	87.66	83.10	13.08	14.0	43.10	9.6	16.3	62.6	2.2	5.6
7	85.12	71.11	14.01	14.2	38.20	7.1	14.5	44.2	2.0	5.0
8	82.00	64.72	10.90	10.2	27.53	4.3	10.4	25.0	1.4	3.6
9	69.92	78.03	11.51	7.9	26.05	4.8	9.9	60.7	1.3	3.4
10	74.16	71.21	12.76	9.8	26.12	4.9	9.9	33.5	1.3	3.4
12	66.08	91.91	12.91	7.9	26.21	6.6	9.9	76.9	1.3	3.4
14	69.92	77.64	10.29	7.0	21.27	4.2	8.1	30.6	1.1	2.8
22	60.92	49.38	9.37	4.9	12.95	1.2	4.9	11.4	0.7	1.7
27	51.18	69.67	11.56	4.2	10.91	2.0	4.1	9.4	0.6	1.4
33	48.56	53.98	12.87	4.2	7.17	1.2	2.7	2.8	0.4	0.9
41	48.10	65.58	11.61	3.8	6.74	1.6	2.6	2.9	0.3	0.9
70	32.36	54.18	9.59	1.4	3.14	0.4	1.2	1.3	0.2	0.4
73	30.28	44.96	11.51	1.5	2.56	0.3	1.0	1.0	0.1	0.3
81	27.24	81.77	8.64	0.9	2.27	0.6	0.9	1.7	0.1	0.3
84	28.80	47.84	11.82	1.4	2.40	0.3	0.9	0.8	0.1	0.3
92	27.24	79.13	9.02	0.9	1.90	0.6	0.7	1.3	0.1	0.2
103	20.90	54.75	12.88	0.8	1.22	0.2	0.5	0.2	0.06	0.2

by Smith & Weedman (1972) from Fabry-Pérot observations in the center of the region shows line profiles with two distinct peaks separated by 45 km s<sup>-1</sup>.

- In the case of 30 Doradus the slit-spectra observations are limited to cover a small fraction of the region. As Chu & Kennicutt (1994) pointed out, the background velocity field they observed in the slit-spectra did not allow them to detect any expanding shell with  $v_{\text{exp}} \leq 50$  km s<sup>-1</sup>, unless it is the dominant emission feature along the line of sight. In our observations we do not have this limitation. If we are observing an expanding shell that does not have a high surface brightness but does occupy a significant fraction of the projected area of the H II region, the best way to distinguish it clearly from the emission of the rest of the H II region is to obtain two-dimensional spectra which can integrate the emission of the shell over a significant fraction of its area and hence can separate it in velocity space from the emission of the rest of the region. This is the process we have followed here to detect the expanding shells in our regions.

Based on the two points explained above we believe that the high velocity features observed in the line profiles of our sample of H II regions are produced by the emission of expanding shells with similar characteristics to those with high luminosities observed in 30 Doradus and NGC 604. Although we do not reject the possibility that there may be other shells inside the H II regions, as they have been indeed detected for these nearby regions, we believe that our collective evidence

demonstrates that these do not contribute significantly to the emission of the high velocity features observed in the integrated line profiles of the H II regions over their full surfaces.

## 5. Feasible driving mechanisms

### 5.1. Stellar winds from the ionizing stars

The winds coming from the ionizing stars interact with the ISM that surrounds the stars. The interaction produces a thin shell of swept-up interstellar medium with less dense material in its interior, which is referred to as a bubble.

The dynamics of this types of bubbles was modelled in considerable detail by Dyson (1980), who found that the kinetic energy of the shell is related to the stellar wind luminosity ( $\dot{E}_{\text{w}} = \frac{1}{2} \dot{M}_{\text{w}} v_{\text{w}}^2$ ),  $E_{\text{k}} = 0.20 \dot{E}_{\text{w}} t$ , where  $t$  is the lifetime for the central ionizing star. Thus, we would expect a ratio between the kinetic energy of the shell and the kinetic energy of the wind of  $\sim 0.2$ .

Assuming a mean lifetime of 10<sup>6</sup> yr for the central ionizing stars, we can estimate their integrated wind energies, using the wind luminosity for an O3(V) spectral type star,  $\log L_{\text{wind}} = 37.08$  (erg s<sup>-1</sup>), given by Leitherer (1998). The values are shown in Col. 8 of Tables 5–7.

In Fig. 8 we show the ratio between the shell kinetic energy and the stellar input wind energy versus logarithmic H $\alpha$  luminosity for the H II region sample. As can be seen in the figure, most of the ratios are in the range 0.25–0.6. The momentum

**Table 6.** The same parameters as in Table 5 but for H II regions NGC 3359.

Region (number)	$R_{\text{shell}}$ (pc)	$v_{\text{shell}}$ (km s <sup>-1</sup> )	$n_{\text{shell}}$ (cm <sup>-3</sup> )	$M_{\text{shell}}$ (10 <sup>4</sup> $M_{\odot}$ )	$N_{\text{eq}}$ (O3(V))	$E_{\text{K}}$ (10 <sup>51</sup> erg)	$E_{\text{wind(O3)}}$ (10 <sup>51</sup> erg)	$E_{\text{turb}}$ (10 <sup>51</sup> erg)	$E_{\text{rad}}$ (10 <sup>54</sup> erg)	$E_{\text{total,rad}}$ (10 <sup>54</sup> erg)
1	97.70	63.63	10.02	13.4	36.81	5.4	14.0	16.8	1.9	4.8
6	69.62	63.97	8.36	56.6	13.97	2.3	5.3	7.1	0.7	1.8
15	68.00	81.91	3.63	2.3	9.42	1.6	3.6	7.6	0.5	1.2
16	68.40	84.56	3.23	2.1	8.55	1.5	3.2	6.4	0.4	1.1
17	52.00	67.31	8.04	3.0	8.11	1.4	3.1	5.8	0.4	1.1
19	63.30	41.85	10.39	5.8	8.03	1.0	3.0	===	0.4	1.0
38	47.70	45.95	7.83	2.5	4.21	0.5	1.6	0.4	0.2	0.6
42	48.66	40.91	8.16	2.7	3.71	0.5	1.4	===	0.2	0.5
44	52.34	59.17	3.88	1.5	3.66	0.5	1.4	0.8	0.2	0.5
45	51.08	43.81	7.76	2.8	3.50	0.8	1.3	===	0.2	0.5
47	45.28	77.29	4.63	1.3	3.42	0.4	1.3	2.0	0.2	0.4
51	37.14	46.73	9.42	1.8	3.23	0.3	1.2	0.05	0.2	0.4
52	34.54	44.97	8.58	1.4	3.18	0.5	1.2	===	0.2	0.4
53	54.62	61.05	3.27	1.3	3.04	0.5	1.2	0.3	0.2	0.4
56	51.64	44.48	6.44	2.4	2.82	0.5	1.1	===	0.1	0.4
83	39.10	41.19	7.29	1.6	1.76	0.3	0.7	===	0.09	0.2
92	36.38	51.98	4.80	0.9	1.51	0.2	0.6	===	0.08	0.2
103	37.14	55.86	4.37	0.8	1.28	0.3	0.5	0.7	0.07	0.2
140	34.54	51.17	6.27	1.0	0.85	0.3	0.3	0.1	0.04	0.1
155	30.84	49.61	4.05	0.5	0.75	0.1	0.3	===	0.04	0.01
192	26.96	55.15	3.86	0.4	0.53	0.1	0.2	0.05	0.03	0.07

**Table 7.** The same parameters as in Tables 5 and 6 but for H II regions NGC 6951.

Region (number)	$R_{\text{shell}}$ (pc)	$v_{\text{shell}}$ (km s <sup>-1</sup> )	$n_{\text{shell}}$ (cm <sup>-3</sup> )	$M_{\text{shell}}$ (10 <sup>4</sup> $M_{\odot}$ )	$N_{\text{eq}}$ (O3(V))	$E_{\text{K}}$ (10 <sup>51</sup> erg)	$E_{\text{wind(O3)}}$ (10 <sup>51</sup> erg)	$E_{\text{turb}}$ (10 <sup>51</sup> erg)	$E_{\text{rad}}$ (10 <sup>54</sup> erg)	$E_{\text{total,rad}}$ (10 <sup>54</sup> erg)
2	66.62	60.93	11.11	6.9	18.11	2.5	6.9	7.1	0.9	2.4
4	54.80	52.08	11.17	4.7	12.61	1.3	4.8	3.8	0.6	1.6
6	54.92	47.09	11.02	4.6	9.17	1.0	3.5	2.5	0.5	1.2
10	51.50	41.73	9.75	3.6	6.74	0.6	2.6	0.2	0.3	0.9
11	52.14	60.47	8.53	3.2	6.48	1.2	2.5	1.8	0.3	0.8
12	52.02	65.41	8.07	3.1	6.27	1.3	2.4	3.5	0.3	0.8
13	52.02	46.71	8.53	3.2	6.26	0.7	2.4	2.4	0.3	0.8
15	49.76	76.36	5.44	1.9	5.38	1.1	2.0	4.2	0.3	0.7
18	48.66	47.62	6.50	2.2	4.58	0.5	1.7	0.6	0.2	0.6
24	37.14	50.95	8.23	1.6	3.29	0.4	1.2	0.4	0.2	0.4
27	40.12	48.45	7.31	1.6	2.79	0.4	1.1	0.2	0.1	0.4
36	36.78	38.62	7.97	1.5	2.31	0.2	0.9	===	0.1	0.3
41	37.34	50.82	8.27	1.6	2.20	0.4	0.8	0.4	0.1	0.3
62	31.22	84.12	6.34	0.9	1.45	0.6	0.5	0.8	0.07	0.2
67	27.52	42.83	8.17	0.9	1.32	0.2	0.5	===	0.07	0.2
69	31.00	78.53	5.79	0.7	1.26	0.5	0.5	1.4	0.07	0.2
75	32.28	51.53	6.45	0.9	1.13	0.2	0.4	0.2	0.06	0.1

of the shell can also be estimated with our observations, using the calculated shell mass and expansion velocity,  $m_s = M_{\text{shell}} \times v_{\text{shell}}$ . The wind momentum can be obtained with the equivalent number of O3(V) type stars given in Col. 6 of Tables 5–7 and the value given by Leitherer (1998) for an O3(V) type star,  $m_w = 7.56 \times 10^{28}$  g cm s<sup>-1</sup>. In Fig. 9, we show the ratio  $\frac{m_s}{m_w}$ , typical values ranges from 15 to 30.

The values of  $\frac{E_k}{E_{\text{wind}}}$  are somewhat higher than the theoretical fraction obtained above. The differences with respect to the theoretical ratio 0.2 could well be due to the uncertainties in obtaining a reliable value for the wind energy input, based on the fact that we are obtaining it from the observed H $\alpha$  luminosity and that a significant fraction of the ionizing luminosity is probably leaking. The observed ratios  $\frac{m_s}{m_w}$  are also affected by

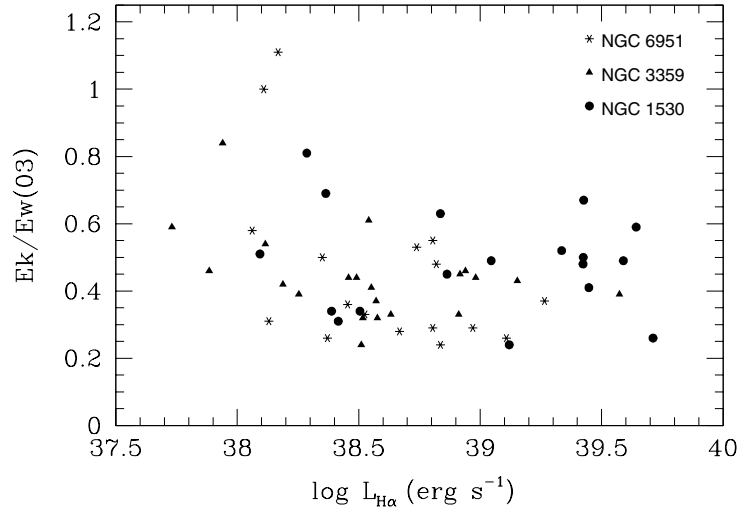


**Fig. 8.** Ratio between the shell kinetic energy and the stellar input wind energy versus logarithmic  $H\alpha$  luminosity for the H II region sample with high velocity features in NGC 1530, NGC 3359 and NGC 6951.

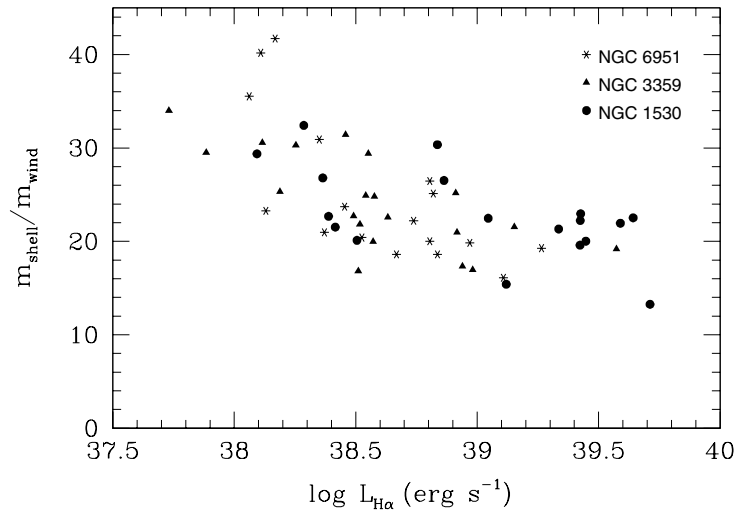


**Fig. 9.** Ratio between the shell momentum and the wind momentum versus logarithmic  $H\alpha$  luminosity.

the difficulties in obtaining a reliable value of the stellar wind momentum using the equivalent number of O3(V) type stars. Using a typical value of the velocity of the shell of  $80 \text{ km s}^{-1}$  and  $v_{\text{wind}} = 3200 \text{ km s}^{-1}$  (Leitherer 1998) for the wind velocity of an O3(V) type star, the expected ratio of  $\frac{m_s}{m_w}$  for the theoretical ratio  $\frac{E_k}{E_{\text{wind}}} = 0.2$  shown above, is  $\frac{m_s}{m_w} \sim 8$ . In any case, the energy and momentum ratios observed show that the stellar winds could be responsible for driving the shell out to radii of order of  $0.2 R_{\text{reg}}$  and that the differences might reasonably be due to the uncertainties in obtaining a reliable value for the wind energy input, as well as the uncertainties entailed in deriving the shell energies and momenta from our observations.

### 5.2. Shells with larger radii

We have investigated further the possibility that the shells might have larger radii than those assumed from nearby H II regions. For two H II regions of each galaxy, we have obtained profiles of  $1 \times 1$  pixels of aperture, located at  $\sim 0.5 R_{\text{reg}}$ .

The H II regions which permit us to obtain these profiles with a significant S:N are among the biggest and most luminous H II regions in the sample. In all of the line profiles extracted as examples, we have found wing features with similar velocities as those found for the best S:N line profiles. This means that for these high luminosity H II regions the expanding shell could be at least at a radius of  $\sim 0.5 R_{\text{reg}}$ .

For these H II regions we have computed the shell electron densities and energy requirements assuming that the shells are located at  $R_s = 0.5 R_{\text{reg}}$ . The results are shown in Table 8. All of the ratios, between the kinetic energy of the shell and the wind energy input,  $E_k/E_{\text{wind}}(\text{O3})$ , shown in Col. 6 of this table have ratios higher than 0.6, in fact the highest ratio is 1.48. These high values are not easily explained with the stellar wind mechanism. Thus, there are probably other mechanisms that can transfer energy to the ISM to produce the kinetic energy of these observed shells.

We suggest two mechanisms which are possible in the context of the known stellar properties of the ionizing clusters, which are supernova energy injection and radiation driving via

**Table 8.** Energetics of the shell for two high luminosity H II regions in each galaxy with a shell radius of  $0.5 R_{\text{reg}}$ . Column 1: H II region number from the catalogue, in parenthesis we show the galaxy they belong to. Column 2: logarithmic  $H\alpha$  luminosity. Column 3: shell radius ( $0.5 R_{\text{reg}}$ ). Column 4: shell expansion velocity. Column 5: mean shell electron density. Column 6: ratio between the kinetic energy of the shell and the wind energy input from the equivalent O3(V) spectral type stars obtained to produce the observed  $H\alpha$  luminosity.

Region (number)	$\log L_{H\alpha}$ ( $\text{erg s}^{-1}$ )	$R_{\text{shell}}$ (pc)	$v_{\text{shell}}$ ( $\text{km s}^{-1}$ )	$N_{\text{shell}}$ ( $\text{cm}^{-3}$ )	$E_K/E_{\text{wind}}(\text{O3})$
6 (N1530)	39.64	219.15	83.10	5.23	1.48
27 (N1530)	39.04	127.95	69.67	4.63	1.23
1 (N3359)	39.57	244.25	63.63	4.01	0.96
19 (N3359)	39.91	158.25	41.85	4.15	0.83
2 (N6951)	39.27	166.50	60.93	4.44	0.93
10 (N6951)	38.84	128.75	41.73	3.90	0.61

dust coupling to the gas following the formalism applied by Elitzur & Ivezić (2001). Supernovae release large amounts of energy, typically of  $E \sim 10^{51}$  erg, but the efficiency of conversion of this energy into kinetic energy in the ISM is  $\sim 4\%$  (Dyson 1980), which is too low to offer a canonical explanation for the shell kinetic energies measured. The stellar radiation from the ionizing stars offers a big energy source which might be available to drive the shell. The stellar radiation from the ionizing stars represents a major energy source which would require only a low coupling efficiency to provide a valid additional input of outflow momentum to the shell. Dust coupling might be one possibility, but the absorption coefficient is known to be low. The photoionization process itself can also contribute. Although the coupling efficiency here is also quite low (Dyson 1980), and this source alone would not drive out material at more than a few times the sound speed, it might well provide an effective incremental contribution which would enhance the effect of the stellar winds (which we have discussed more quantitatively above), enabling the flow to persist out to larger radii with higher overall outflow momentum than that provided by the winds alone. Further consideration of these mechanisms calls for a detailed modelling effort which is beyond the scope of the present paper.

As can be seen from comparison of Cols. 7, 10 and 11 in Tables 5–7, the total radiative energy emitted by the central stars is some three orders of magnitude higher than the kinetic energy of a characteristic expanding shell. In any case, this energy must be taken into account when trying to find an explanation for the high kinetic energies of the shells observed at relatively large radii inside the H II regions. However, in this essentially observational study we can only point the possible mechanisms which might explain the expanding shells located at large radii inside the H II region, for which the stellar winds may not provide energy enough to drive the shell.

## 6. Conclusions

– We have studied the existence of low intensity high velocity components in the integrated line profiles of the H II region populations of three barred spiral galaxies. We have

analyzed the integrated line profiles and extracted a representative sample of spectra which show these components. Down to a limit of  $\log L_{H\alpha} = 38.0$  ( $\text{erg s}^{-1}$ ), we found that 26.77%, 42.0% and 31.63% of the catalogued H II regions in NGC 3359, NGC 6951 and NGC 1530, respectively, show high velocity low intensity features in their integrated line profiles.

- The higher fraction is correlated with a higher S:N ratio in the line profiles, which suggests that at sufficiently high value of S:N all H II regions may well show these wing features, which means that these high velocity features could well exist in most H II region line profiles, and as such provide evidence of a widely distributed phenomenon.
- Based on the mean S:N of the two high velocity components, we have obtained the spectra from the set of line profiles with increasing apertures that best defines the wing features and used them as the representative spectra of each region which characterize the wing parameters.
- The analysis of the fit parameters of the high velocity low intensity features show that parameters of the red and blue component are in the same range of values. The mean values of the Emission Measure for both components are 8.9% of the total  $EM$  of the H II region and the velocity separation ranges from  $40 \text{ km s}^{-1}$  to  $90 \text{ km s}^{-1}$  for our sample of the most luminous H II regions (which cover the high of the luminosity range), with a mean value for each component of  $\langle v_{\text{red}} \rangle = 60.5 \text{ km s}^{-1}$  and  $\langle v_{\text{blue}} \rangle = 59.02 \text{ km s}^{-1}$ . The mean measured velocity dispersions for the red and blue components are  $\langle \sigma_{\text{red}} \rangle = 19.5 \text{ km s}^{-1}$  and  $\langle \sigma_{\text{blue}} \rangle = 17.0 \text{ km s}^{-1}$ , though some line profiles are not fully resolved.
- We interpret the high velocity features as evidence of an expanding shell inside the H II region. The shell expansion velocity is obtained as the mean value of  $v_{\text{red}}$  and  $v_{\text{blue}}$  for each H II region. Based on parameters for the highest luminosity shells observed in the nearby extragalactic H II regions, 30 Doradus and NGC 604, we have estimated the physical parameters and the energetics of the shell of each H II region in our sample.
- We have compared the shell kinetic energy with the kinetic energy of the stellar winds coming from the ionizing stars inside the H II region. For shells with radii  $\sim 0.2 R_{\text{reg}}$ , the ratios we derive between the kinetic energy of the shell and the energies of the stellar winds are rather higher than the expected theoretical ratio 0.2, but the uncertainties in obtaining a reliable value for the wind energy input from the observed  $H\alpha$  luminosity, as well as those inherent in our derivation of the observational values, can well explain the differences. Thus, the ratios obtained imply that stellar winds alone could drive the expanding shells, if these are located within  $\sim 0.2 R_{\text{reg}}$ .
- Some of the most luminous H II regions of our sample show evidence that their expanding shells are located at radii higher than  $\sim 0.5 R_{\text{reg}}$ . For these H II regions the stellar wind mechanism alone may well not be able to explain the observed shell kinetic energies or momenta, implying that there are other mechanisms required to account for the observed properties.

*Acknowledgements.* This work was supported by the Spanish DGES (Dirección General de Enseñanza Superior) via Grants PB91-0525, PB94-1107 and PB97-0219 and by the Ministry of Science and Technology via Grants AYA2001-0435 and AYA2004-08251-C02-01. The WHT is operated on the island of La Palma by the Isaac Newton Group in the Spanish Observatorio del Roque de los Muchachos of the Instituto de Astrofísica de Canarias. We thank the referee, Dr. C. R. O'Dell, for his constructive comments which helped us to make significant improvements to the article.

## References

- Arsenault, R., & Roy, J.-R. 1986, *AJ*, 92, 567  
 Castor, J., McCray, R., & Weaver, R. 1975, *ApJ*, 200, L110  
 Chu, Y.-H., & Kennicutt, R. C. 1994, *ApJ*, 425, 720  
 de Vaucouleurs, G., de Vaucouleurs, A., Corwin, H. G., et al. 1991, *Third Reference Catalogue of Bright Galaxies (RC3)* (New York: Springer)  
 Dyson, J. E. 1980, *Physics of the Interstellar Medium* (New York: John Wiley & Sons), 145  
 Elitzur, M., & Ivezić, Ž. 2001, *MNRAS*, 327, 403  
 Leitherer, C. 1998, *Stellar Astrophysics for the Local Group*, ed. A. Aparicio, A. Herrero, & F. Sánchez (Cambridge: Cambridge University Press), 527  
 Lucy, L. B. 1974, *AJ*, 79, 745  
 Martins, F., Schaerer, D., & Hillier, D. J. 2002, *A&A*, 382, 999  
 Melnick, J., Tenorio-Tagle, G., & Terlevich, R. 1999, *MNRAS*, 302, 677  
 Osterbrock, D. E. 1989, *Astrophysics of Gaseous Nebulae and Active Galactic Nuclei* (Mill Valley: University Science Books)  
 Relaño, M., Beckman, J. E., Zurita, A., Rozas, M., & Giammanco, C. 2004, in press  
 Rosa, M., & Solf, J. 1984, *A&A*, 130, 29  
 Rozas, M., Beckman, J. E., & Knapen, J.-H. 1996, *A&A*, 307, 735  
 Rozas, M., Sabalisk, N., Beckman, J. E., & Knapen, J.-H. 1998, *A&A*, 338, 15  
 Rozas, M., Zurita, A., Beckman, J. E., & Pérez, D. 2000a, *A&AS*, 142, 259  
 Rozas, M., Zurita, A., & Beckman, J. E. 2000b, *A&A*, 354, 823  
 Sabalisk, N. 1995, Ph.D. Thesis, Univ. de Sao Paulo  
 Sabalisk, N., Tenorio-Tagle, G., Castañeda, H., & Muñoz-Tuñón, C. 1995, *ApJ*, 444, 200  
 Smith, M., & Weedman, D. 1972, *ApJ*, 172, 307  
 Spitzer, L. 1978, *Physical Processes in the Interstellar Medium* (New York: J. Wiley & Sons)  
 Tully, R. 1988, *Nearby Galaxies Catalogue* (Cambridge: Cambridge Univ. Press)  
 Weaver, R., McCray, R., Castor, J. Shapiro, P., & Moore, R. 1977, *ApJ*, 218, 377  
 Yang, H., Chu, Y.-H., Skillman, E. D., & Terlevich, R. 1996, *AJ*, 112, 146  
 Vacca, W. D., Garmany, C. D., & Shull, M. 1996, *ApJ*, 460, 914  
 Zurita, A., Relaño, M., Beckman, J. E., & Knapen, J.-H. 2004, *A&A*, 413, 73